ELSEVIER

Dynamics of Atmospheres and Oceans 22 (1995) 19–48

dynamics of atmospheres and oceans

# On the attractors of an intermediate coupled ocean–atmosphere model

Henk A. Dijkstra [a,*], J. David Neelin [b]

[a] *Institute for Marine and Atmospheric Research, Department of Physics and Astronomy, University of Utrecht, Princetonplein 5, 3584 CC Utrecht, Netherlands*

[b] *Department of Atmospheric Sciences, University of California at Los Angeles, 405 Hilgard Ave., Los Angeles, CA 90024, USA*

Received 23 June 1994; revised 15 August 1994; accepted 1 September 1994

**Abstract**

Techniques of numerical bifurcation theory are used to study stationary and periodic solutions of an intermediate coupled model for tropical ocean–atmosphere interaction. The qualitative dynamical behavior is determined for a volume in parameter space spanned by the atmospheric damping length, the coupling parameter, the surface layer feedback strength and the relative adjustment time coefficient. Time integration methods have previously shown much interesting dynamics, including multiple steady states, eastward- or westward-propagating orbits and relaxation oscillations. The present study shows how this dynamics arises in parameter space through the interaction of the different branches of equilibrium solutions and the singularities on these branches. For example, we show that westward-propagating periodic orbits arise through an interaction of two unstable stationary modes and that relaxation oscillations occur through a limit cycle–saddle node interaction. There are several dynamical regimes in the coupled model which are determined by the primary bifurcation structure; this structure depends strongly on the parameters in the model. Although much of the dynamics may be studied in the fast-wave limit, it is shown that ocean wave dynamics introduces additional oscillatory instabilities and how these relate to propagating oscillations.

## 1. Introduction

One of the most striking examples of how coupled processes between atmosphere and ocean introduce temporal variability on different time scales is the interannual climate variability in the equatorial Pacific, particularly the phenomenon known as El Niño–Southern Oscillation (ENSO). This oscillation influ-

* Corresponding author.


*SSDI* 0377-0265(94)00398-X

ences climate on a global scale, for instance causing drought over some areas and enhanced precipitation over others. An extensive treatment of ENSO literature and a physical description of the phenomena have been given by Philander (1989), and possible multiple time scales associated with this variability have been discussed by Rasmusson et al. (1990).

The underlying physics causing this variability has been the subject of many theoretical studies. The main problem is to determine how the time scale(s) is related to individual and essentially coupled processes in the equatorial atmosphere and ocean. One of first models by which the variability was reasonably simulated was that of Zebiak and Cane (1987). Without anomalous external forcing, this coupled model produced recurring warm events that were irregular in both amplitude and spacing, but favoured a 3–4 year period. Zebiak and Cane (1987) indicated three main ingredients of interannual variability: instability of some background state, equilibration of the anomalies (mainly as a result of the thermal structure of the ocean) and a time delay between dynamical changes in the eastern ocean and the associated large-scale wind response.

Instabilities of a spatially constant climatology in a simple model of the coupled ocean–atmosphere were subsequently analysed by Hirst (1986, 1988). Either for a periodic basin or a bounded ocean basin, free equatorial waves (Kelvin and Rossby) can be destabilized through coupling. The importance of linear wave dynamics was later on further explored (Schopf and Suarez, 1988; Suarez and Schopf, 1988; Battisti and Hirst, 1989), leading to the delayed action oscillator model (Schopf and Suarez, 1990). In this metaphor for ENSO dynamics, the key element is the time delay (and thereby a delayed feedback) caused by ocean wave transit effects in a closed basin. Both stability studies and studies on the delayed feedback were later extended using more detailed models (Hirst and Lau, 1990; Cane et al., 1990; Wakata and Sarachik, 1991; Münnich et al., 1991).

In all these studies, processes determining the sea surface temperature (SST) were assumed to occur at a much faster time scale than those associated with wave dynamics (the fast SST limit, $\delta \to \infty$). Neelin (1991), however, showed that interannual oscillations can occur even when ocean wave time scales are very fast compared with those determining the SST field (the fast-wave limit, $\delta \to 0$). It appears that SST (or thermal) modes (which decay when there is no ocean dynamics) are modified through ocean–atmosphere dynamics and can be destabilized through coupled processes.

The connection between modified ocean basin modes and SST modes was explored in a three-part study by Jin and Neelin (1993a,b) and Neelin and Jin (1993), using an equatorial strip approximation for the SST equation. They studied the stability of a prescribed steady (one-way flux corrected) climatology, resembling observations. It appears that in the area in parameter space most in agreement with observational values, there is a merger of a stationary growing SST mode and one of the oscillatory modes originating from wave dynamics. In this way, the spatial structure of the most unstable mode is inherited from the SST mode, whereas ocean dynamics controls to a certain extent the period of oscillation. Interestingly, the stationary SST mode can be continuously 'deformed' to the fast-wave limit and can be studied therefore much more efficiently. This suggests

that much of the dynamical behavior found in the fast-wave limit carries over (at least at strong coupling) to a regime where wave time scales are important.

The nonlinear behavior of the model in the fast-wave limit was explored by Hao et al. (1993). The dominant dynamics is controlled by three dimensionless parameters: the dimensionless atmospheric damping length $\epsilon_a$ which influences the phase difference between sea surface temperature and wind response, the strength of the surface layer feedback ($\delta_s$) through vertical velocities and the coupling parameter $\mu$ controlling the strength of the wind stress–surface layer and wind stress–thermocline feedback. For the weakly nonlinear case, Hao et al. found regimes where multiple steady states exist and regimes with eastward-propagating orbits (owing to thermocline feedback) and westward-propagating orbits (owing to upwelling feedback). At strong coupling, relaxation oscillations are found, where the flow evolves slowly during the warm phase and passes relatively quickly through the cold phase. The relaxation oscillations seem very robust features and have also been found in hybrid coupled general circulation models (GCMs) (Neelin, 1990b).

In this paper, techniques of numerical bifurcation theory are used to map the structure of the equilibrium solutions of the model of Hao et al. (1993). Standard terminology from bifurcation theory is used throughout the text; useful background references are Chow and Hale (1982) and Guckenheimer and Holmes (1983). Where space permits, elaboration is provided for less common terms. The aim of these explorations is to show how behavior in each part of parameter space is related to behavior in other parts. For instance, as the coupling coefficient is increased, the coupled system can go unstable either to a stationary mode (giving a transcritical bifurcation) or to an oscillatory mode (Hopf bifurcation). These are codimension one bifurcations, as they fundamentally involve only a single parameter. By tracing how each of these bifurcations evolve as a second parameter (such as $\delta_s$ or $\epsilon_a$) is changed, it is possible to understand how two stationary instabilities are connected to an oscillatory instability in neighboring regions. Such connections at intersections of paths of codimension one bifurcations fundamentally involve two parameters and are known as codimension two bifurcations. These form the boundaries of qualitative different dynamical behavior in parameter space (Guckenheimer and Holmes, 1983). Locally around these singularities more complicated behavior (torus bifurcations or relaxation oscillations) may occur.

After presenting the model in Section 2, Section 3 presents results in the fast-wave limit which outline the connections between regimes with zonally propagating SST anomalies and regimes with multiple stationary solutions. The relation between relaxation oscillations and multiple stationary solutions is discussed in Section 4. Section 5 examines the connection to regimes with realistic time scales of ocean dynamics, with conclusions and discussion in Section 6.

## 2. Model formulation

### *2.1. Model*

The intermediate model used in this study is similar to that used by Hao et al. (1993), and only the essential features are described. The ocean model consists of a

modified shallow water model with an embedded mixed surface layer (of fixed depth $H_1$) and an underlying shallow water layer (of mean depth $H_2$). The zonal velocity field in the mixed layer $u_1$ can be written as the sum of the surface layer velocity $u_s$ and the mean velocity over both layers $u$, i.e. $u_1 = u_s + u$. A similar decomposition holds for the other dependent quantities.

Apart from meridional advection, two vertical processes (thermocline deviations and upwelling) determine the sea surface temperature T. Because the strongest surface temperature response to these processes is confined to a fairly narrow band along the equator, a simple equation for the sea surface temperature can be used (Hao et al., 1993):

$$\begin{aligned} \mathrm{T}_t = & -\mathscr{H}(w_1)\left(w_1/\tilde{H}\right)\left[\mathrm{T} - \mathrm{T}_s(h)\right] + \mathscr{H}(-v_N)(2v_N/L_y)(\mathrm{T} - \mathrm{T}_N) \\ & - \epsilon_T(\mathrm{T} - \mathrm{T}_0) - u_1\mathrm{T}_x \end{aligned} \tag{1}$$

where $\mathscr{H}$ is a continuous approximation of the Heaviside function.

The first term on the right-hand side models the heat flux owing to upwelling through total vertical velocity $w_1$ and approximate (over a certain depth $\tilde{H}$) vertical temperature gradient $(\mathrm{T} - \mathrm{T}_s(h))/\tilde{H}$. The subsurface temperature ($\mathrm{T}_s$) depends in a nonlinear way on thermocline deviations and is parameterized in the same way (see Appendix A) as done by Hao et al. (1993). The second term on the right-hand side of (1) represents meridional inwelling through off-equatorial (over a length scale $L_y$ equal to the equatorial Rossby deformation radius) surface layer meridional velocity $v_N$ and temperature $\mathrm{T}_N$. The system can switch 'continuously' between upwelling and downwelling (and corresponding meridional inwelling). The fourth term in (1) represents Newtonian cooling with damping time scale $\epsilon_T$; $\mathrm{T}_0$ is the equilibrium temperature in absence of dynamics. The last term in (1) models zonal advection.

By prescribing the velocities and the thermocline depth in the ocean (for instance by using climatological values) a reference steady state $\overline{\mathrm{T}}$ is obtained from (1). Sea surface temperature anomalies from this reference state force an atmospheric wind field which has been described by a Gill type model (Gill, 1980), characterized by the velocity of the first baroclinic Kelvin mode $c_a$ and by a damping coefficient $D_M$. The heating field driving the atmospheric winds is assumed proportional to the SST anomalies with proportionality factor $\alpha_T$. In the equatorial strip, the wind response is mainly zonal and the zonal wind field can be written as $U = A(\mathrm{T} - \overline{\mathrm{T}})$, where $A$ indicates the atmosphere model.

The ocean in its turn is forced by this anomalous wind field, and the zonal wind stress is assumed proportional to the wind field $U$ with proportionality factor $\gamma_\tau$. In addition, it has a forcing component $\tau_0 F(x)$ independent of SST changes which is used to generate the reference state $\overline{\mathrm{T}}$. With $H = H_1 + H_2$, the wind forcing in the equatorial strip is therefore given by

$$\tau/(\rho H) = \tau_0 F(x) + \gamma_\tau U \tag{2}$$

The zonal surface layer velocity is parameterized (see Appendix A) as done by Hao et al. (1993), as being proportional to zonal wind stress. The other velocity

components are determined by continuity. The mean velocity field satisfies a reduced gravity model in a basin of length $L$ on the equatorial $\beta$-plane, characterized by the velocity of the first baroclinic Kelvin mode $c_0$ and a Rayleigh friction coefficient $a_M$. These equations are made dimensionless by using scales $c_0$, $L/c_0$, $H_1c_0/L$, $c_0L_y/L$, $L$, $L_y$, $H$ and $\Delta T = 1°C$ for zonal velocity, time, vertical velocity, meridional velocity, zonal and meridional length, thermocline depth and temperature, respectively. In the long wave approximation, the dimensionless equations become

$$\delta u_t - yv + h_x + ru = F_0F(x) + \mu A(T;x) \tag{3a}$$

$$yu + h_y = 0 \tag{3b}$$

$$\delta h_t + rh + (u_x + v_y) = 0 \tag{3c}$$

with $r = a_ML/c_0$, $F_0 = \tau_0L/c_0^2$ and $T = T - \overline{T}$. The parameter $\mu$ is the coupling parameter given by $\mu = \alpha_T\gamma_\tau\Delta TL^2/(c_0^2c_a^2)$. The atmosphere model becomes

$$A(T;\, x) = \tfrac{3}{2}\exp(3\epsilon_a x)\int_x^1 \exp(-3\epsilon_a s)T(s)\,\mathrm{d}s - \tfrac{1}{2}\exp(-\epsilon_a x)\int_0^x \exp(\epsilon_a s)T(s)\,\mathrm{d}s \tag{3d}$$

with $\epsilon_a = D_ML/c_a$.

The nondimensional variable $\delta$ is introduced to study the effect of wave time scales on the stability of the steady states. With the time scaling as above, $\delta = 1$; the fast-wave limit is obtained as $\delta \to 0$ and the fast SST limit as $\delta \to \infty$.

The steady-state mean velocity fields and thermocline displacements in (3) can be solved in terms of $T$ (see Appendix A) and finally an integro-differential equation for the temperature deviation $T$ from the reference state $\overline{T}$ is obtained, i.e.

$$\begin{aligned} &-\{[\delta_F^2F(x) + u + \mu\delta_u A(T;\, x)]\mathrm{T}_x + \epsilon_w(\mathrm{T} - \mathrm{T}_0) \\ &+\mathscr{H}(w_1)[-\alpha rh + \alpha\delta_u\mu A_x(T;\, x) - \delta_s\mu A(T;x) \\ &+\alpha\delta_F^2F'(x) - \delta_F^1F(x)][\mathrm{T} - \mathrm{T}_s(h)] \\ &+\mathscr{H}(-v_N)\alpha^{-1}[\delta_s\mu A(T;\, x) + \delta_F^1F(x)](\mathrm{T} - \mathrm{T}_N)\} = \mathrm{T}_t \end{aligned} \tag{4}$$

where the dimensionless parameters are defined in Appendix A. Most parameters in Eq. (4) will be kept constant and their 'best' values are given in Table 1. We will study the solutions of the steady equation, Eq. (4), along with their linear stability in a four-dimensional parameter space spanned by $\epsilon_a$, $\mu$, $\delta_s$ and $\delta$. The physical significance of these parameters is repeated for convenience: $\mu$ is the relative coupling coefficient—the strength of the wind stress feedback from the atmosphere to the ocean; $\delta_s$ is the surface layer coefficient—the ratio of the time scale of SST change by vertical-mean current and thermocline feedbacks to the time scale of SST change by coupled current perturbations associated with the active surface layer; $\epsilon_a$ is the atmospheric damping length, relative to the zonal basin

Table 1
Values of dimensional parameters for the standard case

| | | |
|---|---|---|
| $H_1 = \tilde{H} = 50$ (m) | $\epsilon_T = 9.25\times10^{-8}$ ($s^{-1}$) | $b_w = 1.026\times10^2$ (s) |
| $H = 200$ (m) | $L = 1.5\times10^7$ (m) | $\tau_0 = 2.667\times10^{-7}$ (m $s^{-2}$) |
| $T_0 = 30$ (°C) | $c_a = 30$ (m $s^{-1}$) | $T_{s0} = 22$ (°C) |
| $T_N = 30$ (°C) | $\Delta T = 1$ (°C) | $h_0 = 25$ (m) |
| $c_0 = 2$ (m $s^{-1}$) | $D_M = 5.0\times10^{-6}$ ($s^{-1}$) | $H^* = 30$ (m) |
| $a_M = 1.3\times10^{-8}$ ($s^{-1}$) | | |
| Fixed dimensionless parameters in (4): | | |
| $\delta_F^1 = 4.104$ | $\eta_1 = 6.667$ | $\eta_2 = 0.833$ |
| $F_0 = 1.0$ | $\alpha = 1.0$ | $\epsilon = 10^{-4}$ |
| $\epsilon_w = 0.694$ | | |

scale; $\delta$ is the relative adjustment time coefficient—it measures the ratio of the time scale of oceanic adjustment (in the zonal direction) by wave dynamics to the time scale of adjustment of SST by coupled feedback and damping processes.

### 2.2. Basic states, linear stability and numerical methods

The reference state $\overline{T}(x)$ is obtained by putting $T = 0$ and prescribing $F(x)$ in (4). In this way, the reference state is a one-way flux corrected climatology and the equation determining this state is

$$a_1(x)\overline{T}' + d_1(x)\overline{T} = d_2(x) \tag{5}$$

where the coefficients $a_1(x)$, $d_1(x)$ and $d_2(x)$ are given in Appendix B and the prime denotes differentiation to $x$. As a boundary condition, we assume no heat flux through the western boundary; hence $\overline{T}'(0) = 0$. As done by Hao et al. (1993), we take for $F(x)$

$$F(x) = 0.6\{0.12 - \cos^2[(x - x_0)\pi/(2x_0)]\}, \quad x_0 = 0.57 \tag{6}$$

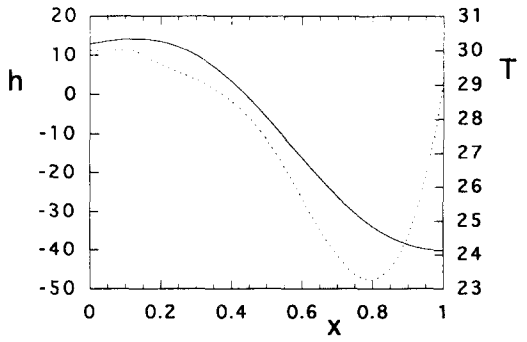


Fig. 1. Climatological temperature $\overline{T}$ (dotted line) and thermocline field $\overline{h}$ (continuous line) obtained with standard values of parameters.

The climatology ($\overline{h}$, $\overline{T}$) is shown in Fig. 1 for the standard values of the parameters as in Table 1. Upwelling occurs over most of the basin except on a small interval near the western boundary. The thermocline is shallow at the east and larger than the equilibrium value in the west. This gives a moderate cold tongue in the eastern part of the basin; the climatology is similar to that computed by Hao et al. (1993).

To study the linear stability of a particular basic state $\overline{T}(x)$, we consider deviations from this basic state through

$$T(x,t) = \overline{T}(x) + \hat{T}(x,t) \tag{7}$$

with similar expressions for the other ocean and atmosphere dependent quantities. Substitution into the governing equations leads to the evolution equations for the disturbances, i.e. the integro-differential equation for $\hat{T}(x, t)$ becomes

$$\begin{aligned}\hat{T}_t(x, t) = {} & a(x)\hat{u}(\hat{T};x, t) + \gamma(x)\hat{h}(\hat{T};x, t) - \epsilon_w(x)\hat{T}(x, t) \\ & + \mu\delta_s b(x)\hat{A}(\hat{T};x, t) - \mu\delta_u c(x)\hat{A}_x(\hat{T}; x, t) \\ & - \mu\delta_u d(x)\hat{A}(\hat{T};x, t)\end{aligned} \tag{8}$$

where the coefficient functions $b(x)$, $\gamma(x)$ and $\epsilon_w(x)$ are given in Appendix C. The linearized equations around the basic state $\overline{T}(x)$ admit solutions $\hat{T}(x, t) = \tilde{T}(x)e^{\sigma t}$, $\hat{A}(\hat{T}; x, t) = \tilde{A}(\tilde{T}; x)e^{\sigma t}$, etc. The solutions $\tilde{u}$ and $\tilde{h}$ at the equator can be expressed in terms of $\tilde{T}$ using Green's functions (Neelin and Jin, 1993). In this way, (8) leads to an eigenvalue problem with eigensolution ($\sigma$, $\tilde{T}$).

The steady equation (4) is discretized on a regular grid which leads to a system of nonlinear algebraic equations. The bifurcation package AUTO (Doedel, 1980) is used to trace branches of steady states as one of the parameters is varied. The AUTO package is also used to solve the eigenvalue problem (8). Details on the implementation in AUTO are provided in Appendix D.

## 3. Results: fast-wave limit ($\delta \to 0$)

The fast-wave limit is not the most realistic part of the parameter space, as time scales of subsurface dynamical adjustment in the ocean are assumed to occur very fast. However, it serves as a good place to begin unravelling many aspects of the bifurcation diagram. Stationary states are the same as in the full model, and a good prototype is provided for oscillations which have propagation of anomalies of SST, wind, currents, etc., along the equator. In the following sections, we focus on the ways in which the topology of the bifurcation diagram as a function of coupling changes when other parameters are varied and how this can be used to make sense of connections among different regimes of behavior. One recurring theme is the way that pairs of stationary modes in one part of parameter space evolve into oscillatory modes in neighboring regions, a process sometimes referred to as mode

competition (Golubitsky et al., 1988, Chapter XIX). Implications of these connections are further discussed in Section 6, along with a recapitulation of physical processes associated with these mergers.

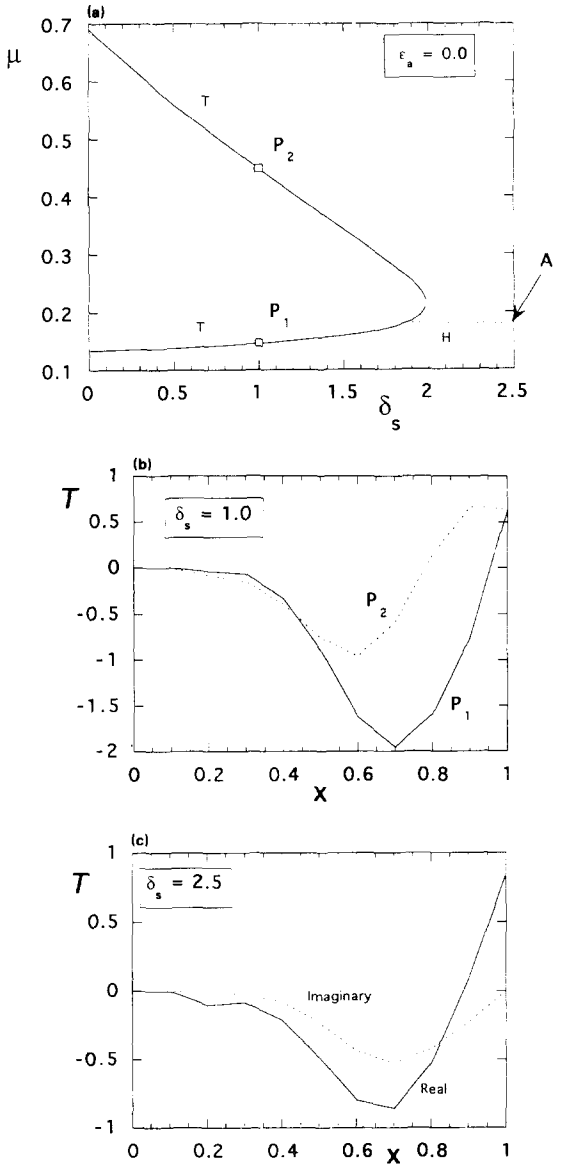


Fig. 2. (a) The paths of primary bifurcation points in the ($\delta_s$, $\mu$) plane (T, transcritical bifurcation points; H, Hopf bifurcation points) for $\epsilon_a = 0$. (b) SST anomaly as a function of longitude for eigenfunctions at neutral stability for $\delta_s = 1.0$ at locations $P_1$ and $P_2$ indicated in (a). (c) SST anomaly for the complex eigenfunction (two phases of the westward-propagating oscillation) at neutral stability at Point A in (a).

### 3.1. Connection between stationary and westward-propagating modes, $\epsilon_a = 0$

The simplest case to consider is $\epsilon_a = 0$, which corresponds to a broad scale atmospheric response to SST anomalies. The paths of primary bifurcation points in the $(\delta_s,\mu)$ plane are shown for $\epsilon_a = 0$ in Fig. 2(a). Here 'primary' refers, throughout the text, to bifurcations from the climatological state (shown in Fig. 1). Up to $\delta_s \approx 1.8$, the first two primary bifurcation points are transcritical (T). For instance, at $\delta_s = 1$, the climatology is unstable to one stationary mode (a real eigenvector) for $\mu > \mu(P_1)$ but unstable to two stationary modes for $\mu > \mu(P_2)$. The spatial patterns of both modes are shown in Fig. 2(b) (at the points $P_1$ and $P_2$). For larger $\delta_s$, a Hopf bifurcation (H) is the first primary bifurcation. For instance, at $\delta_s = 2.5$, the climatology is unstable to an oscillatory mode for $\mu > \mu(A)$. This is a complex eigenvector of which the structure is shown in Fig. 2(c). It propagates westward with time because the maximum westerly wind response is to the left of the maximum (positive) SST anomaly. These mechanisms have been discussed in more detail by Hao et al. (1993). At the transition near $\delta_s = 1.9$, one of the stationary modes becomes the real part and the other mode the imaginary part of this complex eigenvector; this merger of two stationary modes to produce oscillatory behavior is an example of mode competition (Golubitsky et al., 1988).

There is a small region in $\delta_s$ (approximately from $\delta_s = 1.9$ to $\delta_s = 2.0$) where three singularities occur in a small interval of $\mu$. In this region, the frequency associated with the complex pair of eigenvalues which crosses the imaginary axis (at H) goes to zero with increasing $\mu$. Of the remaining two unstable modes, one of them stabilizes in the first transcritical bifurcation but destabilizes again at the second. The other mode remains unstable with increasing $\mu$.

In correspondence with Fig. 2(a), the bifurcation picture for $\epsilon_a = 0$, $\delta_s = 1.0$ in Fig. 3 shows two transcritical primary bifurcation points, $P_1$ and $P_2$. On the vertical

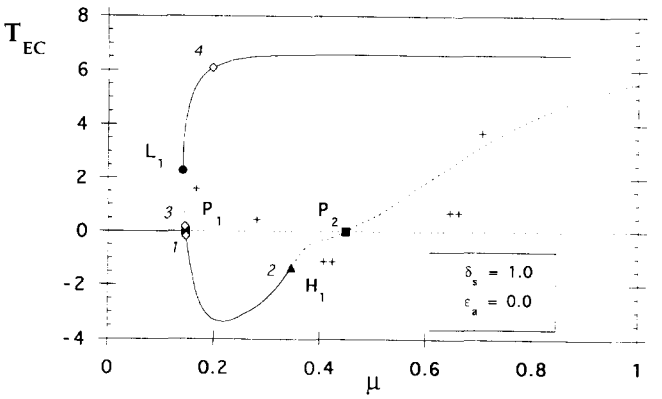


Fig. 3. Bifurcation picture for $\epsilon_a = 0$, $\delta_s = 1.0$. On the vertical axis, the temperature $T_{EC} = T(x = 0.7)$ is plotted. Continuous (dashed) lines indicate stable (unstable) branches. L, Limit points; P, transcritical primary bifurcations; H, Hopf bifurcations.

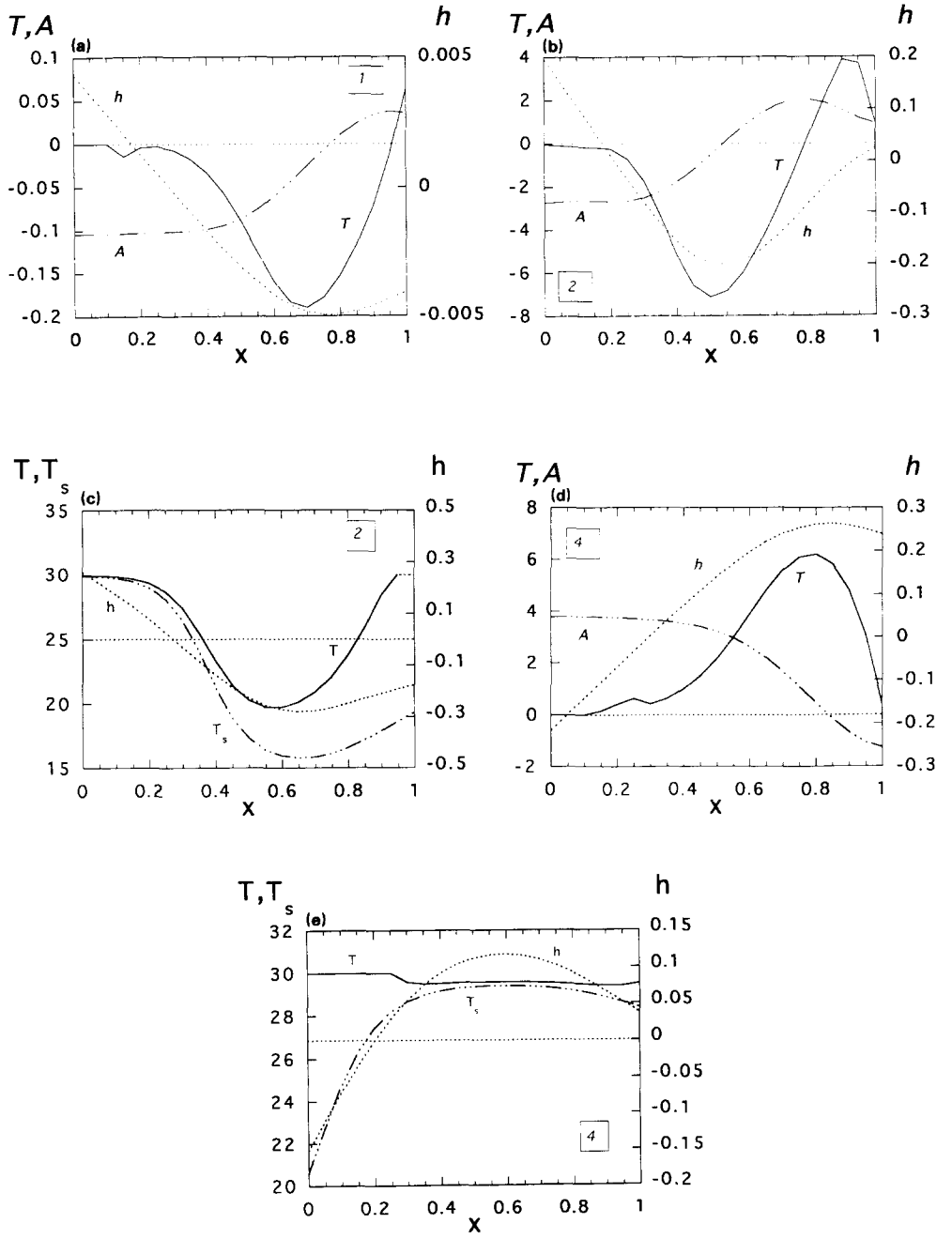


Fig. 4. (a) Spatial structure of perturbation temperature field $T$, thermocline displacement $h$ and wind field $A$ at Point 1 in Fig. 3. (b) Same as (a), but at Point 2. (c) Spatial structure of the total fields T, h and $T_s$ at Point 2 in Fig. 3. (d) Same as (a), but at Point 4. (e) Same as (b), but at Point 4.

axis, the temperature $T_{EC} = T$ ($x = 0.7$) of an index point situated in the eastern central Pacific, is plotted. This is a useful indicator of the dynamics, because the different branches are easily distinguished. However, when branches intersect (using this indicator) there is not always a singularity. Therefore, markers along the branch indicate singularities (solid squares for a transcritical bifurcation, solid triangles for a Hopf bifurcation and solid circles for a limit point) on branches. At points marked with open squares, solutions are presented in subsequent figures. Solid (dashed) lines indicate stable (unstable) steady states. The plus signs indicate the number of eigenvalues with a positive real part.

The bifurcation points $P_1$ and $P_2$ are connected through a branch of steady states which is stable from $P_1$ up to the secondary Hopf bifurcation point, $H_1$, at $\mu = 0.346$. The structure of the perturbation temperature field $T$, the thermocline perturbation $h$ and the wind field $A$ are shown for Point 1 on this branch in Fig. 4(a). Near $P_1$, $h$ is positive (negative) in the west (east), strengthening the cold tongue of the climatology. The total fields are still very similar to the climatology as shown in Fig. 1, as the amplitude of the perturbation is small.

At Point 2 on the lower branch in Fig. 3, the perturbation fields and the total fields T, h and $T_s$ are given in Figs. 4(b) and 4(c). With increasing coupling, the (positive) maximum of the wind perturbation shifts to the west. This is accompanied by a westward shift of the maximum of vertical perturbation downwelling, and thus the (negative) mimimum of the temperature perturbation also shifts westward, whereas a (positive) maximum of $T$ develops in the easternmost part of the basin. Although it is not clear exactly why, it is notable that at the Hopf bifurcation, the thermocline perturbation becomes positive in the eastern part of the basin (Fig. 4(b)). The subsurface temperature is increased, and hence the temperature in the eastern part of the basin is increased (Fig. 4(c)).

The first upper branch in Fig. 3 is unstable from $P_1$ up to the limit point $L_1$ but thereafter stabilizes with increasing coupling and remains stable certainly up to $\mu = 1.0$. The most unstable temperature perturbation at Point 3 on this branch has the same spatial structure as that in Fig. 4(a), but opposite sign. It is positive over most of the basin except in the east, with westerly winds tending to deepen the thermocline in the east and to reduce upwelling. Again, the total fields are similar to that in Fig. 1.

For larger coupling, these feedbacks increase until the total temperature field T approaches the equilibrium temperature $T_0$ (Figs. 4(d) and 4(e)). As the value of $\mu$ at $L_1$ is smaller than that at $P_1$, there exists a stable steady state already below the critical value (the value where instability occurs) of the coupling. Hence, a small region of subcritical instability exists where the climatology can change to another steady state through finite amplitude perturbations, although it is linearly stable. The upper branch from $P_2$ in Fig. 3, corresponding to a $T$ positive (negative) in the middle (east) of the basin, remains unstable.

The path of the Hopf bifurcation labelled $H_1$ in Fig. 3 (with associated frequency $\nu$) and the limit point $L_1$ are shown as a function of $\mu$ and $\delta_s$ in Fig. 5(a). The path through $H_1$ intersects the double zero singularity with zero frequency (as shown in Fig. 2(a)) and thus connects up to the branch of primary Hopf

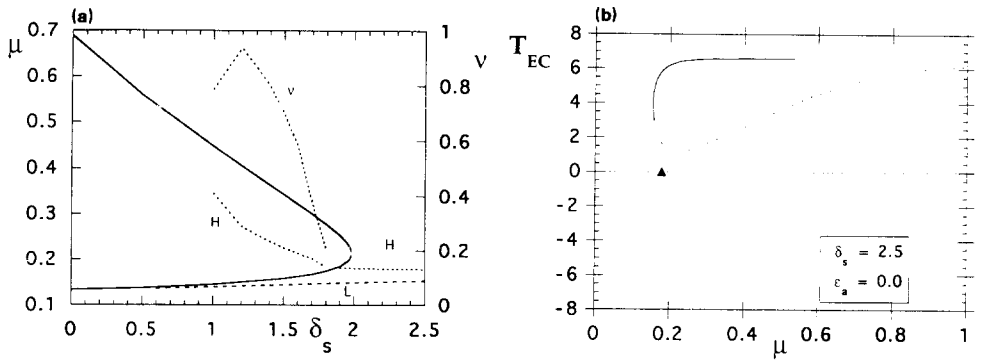


Fig. 5. (a) Paths of secondary singularities (H, Hopf bifurcation point; L, limit point) in the ($\delta_s$, $\mu$) plane for $\epsilon_a = 0$ added to paths of primary singularities (as in Fig. 2(a)). The frequency $\nu$ of the Hopf bifurcations for $\delta_s < 1.8$ is also shown (values given on right ordinate). (b) Bifurcation picture for $\delta_s = 2.5$, $\epsilon_a = 0$.

bifurcation points at larger $\delta_s$. In this way, oscillatory instabilities of the steady states on the (cold) branch $P_1$–$H_1$ relate to those of the flux corrected climatology. As we know from Fig. 2(a), the westward-propagating instabilities of the flux corrected climatology are associated with an increasing competition of the two unstable modes (corresponding to the eigenvectors at $P_1$ and $P_2$) as $\delta_s$ is increased. Fig. 5(a) indicates that steady states on the cold branch (which depend on coupling) go unstable to oscillatory instabilities at smaller values of $\delta_s$, but the relationship of oscillatory and stationary instabilities (the mode competition) is the same.

Because the limit point $L_1$ still exists for $\delta_s > 1.86$, the warm (near equilibrium) state remains stable in a parameter regime where the original climatology would only go unstable through oscillatory instabilities. To clearly demonstrate this, the bifurcation picture for $\epsilon_a = 0.0$, $\delta_s = 2.5$ is presented in Fig. 5(b). The appearance of the isolated branch in Fig. 5(b) is interesting because steady-state switching occurs even though there is no stationary bifurcation at all.

A branch of stable supercritical periodic orbits is found near the point A in Fig. 2(a) at $\delta_s = 2.5$. The spatial structure of the SST anomaly on this orbit is shown in Fig. 6. The maximum field value and the period of the oscillation are given in the caption. The oscillation is nearly standing in the central part of the basin, whereas there is slight westward propagation in the east. The anomaly extends nearly over the whole basin. The spatial structure of the modes which span the orbit are those in Fig. 2(c).

The branch of periodic orbits coming from the (subcritical) Hopf bifurcation $H_1$ in Fig. 3 is unstable. The spatial structure of the orbit is similar to that in Fig. 6; the maximum amplitude is slightly shifted to the west. Hence, as the periodic orbits go through the double zero singularity near $\delta_s = 1.9$ in Fig. 5(a), the Hopf bifurcations go from supercritical to subcritical with decreasing $\delta_s$ and therefore the periodic orbits become unstable. Periodic westward-propagating orbits only

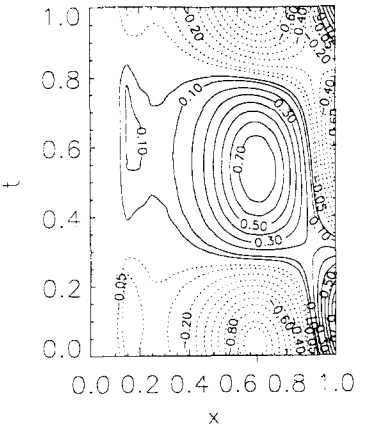


Fig. 6. Time longitude structure of the SST anomaly for the periodic orbit (period $p = 2.91$ year) at Point A in Fig. 2(a) ($\epsilon_a = 0$, $\delta_s = 2.5$). Contour values are scaled with respect to SST maximum, $T_m = 8.99 \times 10^{-1}$.

arise through instability of the climatology at large $\delta_s$, i.e. through surface-layer feedback.

### 3.2. Dependence on atmospheric damping parameter $\epsilon_a$

Hao et al. (1993) also found eastward-propagating instabilities for vanishing zero surface layer feedback ($\delta_s = 0$) at larger $\epsilon_a$. In this section, the zonal scale characterizing the nonlocal atmospheric response is varied (by varying $\epsilon_a$) to see how the eastward-propagating oscillatory instabilities arise. Another point of study is whether the mode competition as demonstrated in the previous section between stationary instabilities leading to westward-propagating oscillatory instabilities is robust.

The primary bifurcation structure of Fig. 2(a) remains qualitatively the same up to $\epsilon_a \approx 1.25$ (Fig. 7(a)). A second set of modes now becomes unstable at higher coupling. At this value of $\epsilon_a$, the two sets of modes do not interact. The set seen at lower coupling ($\mu \leqslant 1$ in Fig. 7(a)) is the same as that of Fig. 2(a); the second set has similar behavior with stationary modes at lower $\delta_s$ combining to give oscillatory (westward-propagating) solutions at larger $\delta_s$. At larger $\epsilon_a$, they do interact and give the picture of Fig. 7(b) at $\epsilon_a = 1.75$. The upper stationary branch from the second set now connects to the upper stationary branch of the first set at a double zero singularity. At even larger $\epsilon_a$, also the lower branches of both modes connect in a double zero singularity giving the picture for $\epsilon_a = 2.5$ in Fig. 7(c). At $\epsilon_a = 2.5$, oscillatory instabilities take over at small $\delta_s$ and the regime where the two steady modes are most unstable is restricted to a small interval in $\delta_s$. For intermediate $\delta_s$, the primary bifurcation point is transcritical, whereas the second one is a Hopf bifurcation. At even larger $\delta_s$, the Hopf bifurcation crosses the transcritical one

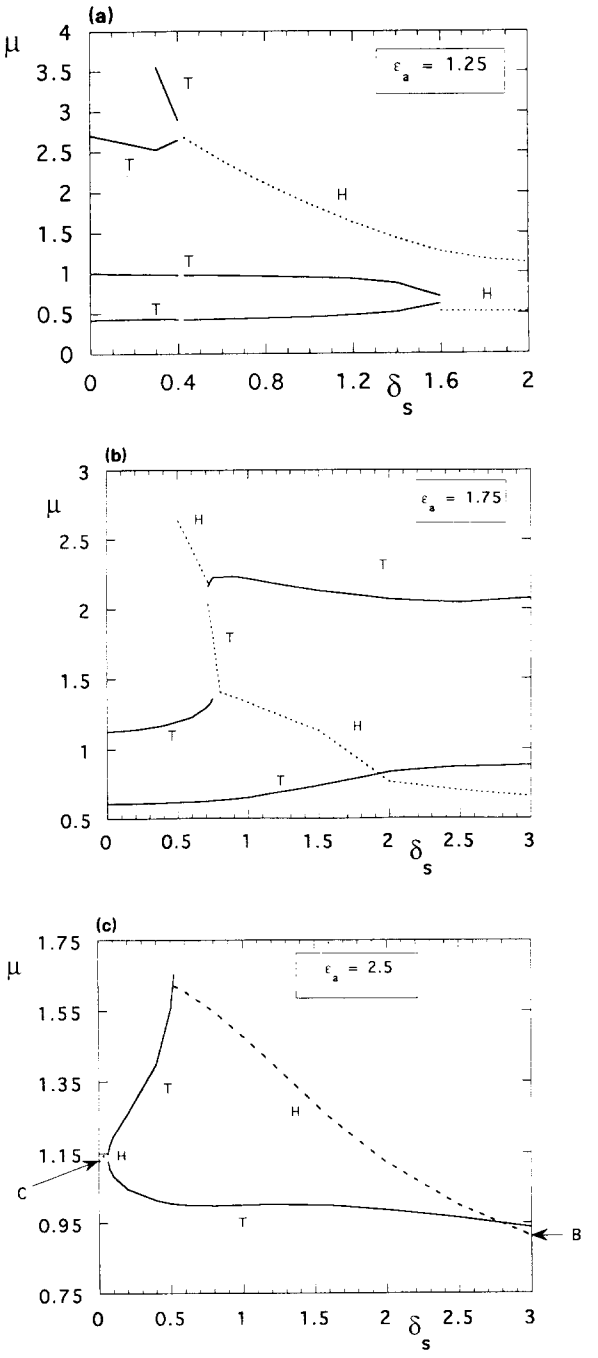


Fig. 7. Primary bifurcation structures for several values of $\epsilon_a$ (notation as in Fig. 2). (a) $\epsilon_a = 1.25$. (b) $\epsilon_a = 1.75$. (c) $\epsilon_a = 2.5$.

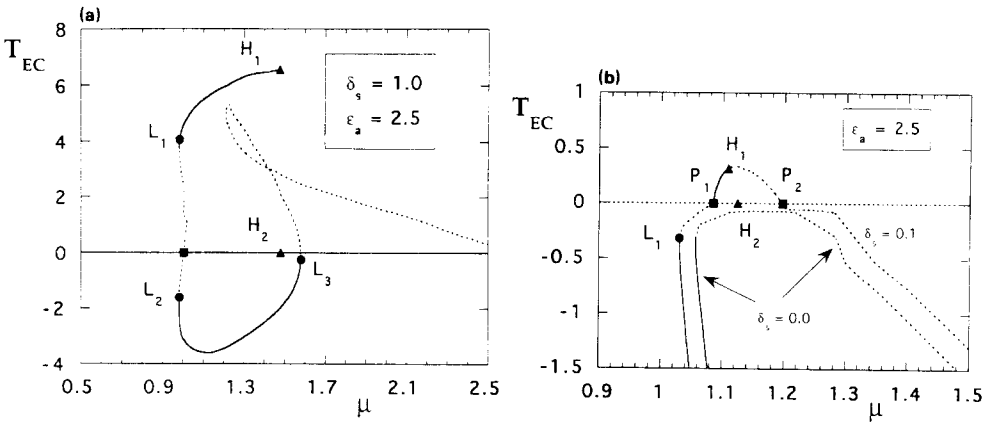


Fig. 8. Bifurcation pictures (notation as in Fig. 3). (a) For $\epsilon_a = 2.5$ and $\delta_s = 1.0$. (b) for $\epsilon_a = 2.5$ and two values of $\delta_s$ (0.0 and 0.1).

and becomes the first primary bifurcation. A Hopf–steady-state interaction (Golubitsky et al., 1988) occurs at about $\delta_s \approx 2.78$, $\mu \approx 0.95$. Locally around this codimension-two singularity, torus bifurcations can be expected (Langford, 1979). These were indeed found at $\mu$ values slightly higher than that at the singularity. The quasi-periodic solution (where the periodic orbit coming from the first Hopf bifurcation is modulated by a lower frequency) turned out to exist only over a very small interval of coupling. Although it illustrates that quasi-periodic behavior can exist in the fast-wave limit, it is exotic and will not be discussed further.

Most important from Fig. 7 is that with increasing $\epsilon_a$, modes originally (at $\epsilon_a = 0$) from two different sets interact. The coalescence of two stationary modes to form an oscillatory mode in Fig. 7(c) at small $\delta_s$ is noteworthy because this is an eastward-propagating mode, as discussed below.

### 3.3. Connection between stationary modes and eastward-propagating modes

In this section, mode competition is shown also to be the underlying structural relation between the eastward-propagating oscillatory instabilities and stationary instabilities. Figs. 8(a) and 8(b) show bifurcation diagrams corresponding to slices through Fig. 7(c) at two values of $\delta_s$. Fig. 8(a) shows the case that applies for relatively large $\delta_s$, and Fig. 8(b) shows two cases near the region of eastward-propagating instabilities at low $\delta_s$. For $\epsilon_a = 2.5$, $\delta_s = 1.0$, it is observed from the bifurcation diagram in Fig. 8(a) that the first upper branch is now supercritical and the lower branch subcritical. Several limit points (not explicitly shown) appear on the branch $P_1$–$L_1$, giving rise to small intervals in $\mu$ where the branch is stable. After the final limit point $L_1$ the upper branch remains stable up to the Hopf bifurcation point H at $\mu \approx 1.4$. The lower branch is stable from $L_2$ up to the limit point $L_3$ and it eventually connects up with a transcritical primary bifurcation point at larger $\mu$ ($\mu = 2.7$). In correspondence to previous results in Hao et al.

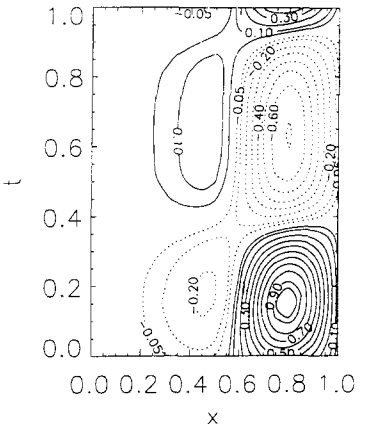


Fig. 9. Time longitude structure of the SST field of the periodic orbit (period 13.3 years) at Point C in Fig. 7(c) ($\epsilon_a = 2.5$, $\delta_s = 0.0$). Contours scaled as in Fig. 6, with $T_m = 8.71 \times 10^{-2}$.

(1993) three stable steady states are found at this (intermediate) value of $\delta_s$. The results of their 'toy model' are basically correct, although the details on the secondary bifurcation structure are different.

If $\delta_s$ is decreased down to $\delta_s \approx 0.525$, the bifurcation pictures remain qualitatively the same as that in Fig. 8(a). For $0.05 < \delta_s < 0.525$, the picture is qualitatively the same as that for $\delta_s = 0.1$ presented in Fig. 8(b). Again, both primary bifurcation points are transcritical, there is a secondary Hopf bifurcation ($H_1$) at the upper branch and a limit point ($L_1$) on the lower branch. The path of the Hopf bifurcation is connected to the eastward-propagating instabilities of the climatology at smaller $\delta_s$ (see Fig. 7(c)) and moves to $H_2$ at $\delta_s = 0$. A stable branch of eastward-propagating orbits arising at this point is shown in Fig. 9 (near Point C in Fig. 7(c)). Here, the oscillation is nearly standing in the eastern part of the basin whereas it is slightly propagating in the central part of the basin. The period $p$ ($p = 13.3$ years) is rather large and, as expected, sensitive to the parameters in the subsurface temperature parameterization. As $\delta_s \to 0$, the branch of steady states in Fig. 8(b) has disconnected from the climatology and (as in Fig. 5(b)) again an isolated branch of stable states (a cold state) appears. The connection between stationary and eastward-propagating orbits is therefore similar to that between stationary and westward-propagating orbits. The oscillatory instabilities near $\delta_s = 0$ (Fig. 7(c)) are associated with the competition of two stationary modes which were most unstable at slightly larger $\delta_s$. The spatial structure of the stationary mode that goes unstable near the point $P_1$ in Fig. 8(b) resembles the structure during the extreme phase ($t = 0.2$ or $t = 0.7$ in Fig. 9), whereas the second stationary mode ($P_2$ in Fig. 8(b)) resembles the transition phase in Fig. 9. In fact, if one refers back to the sequence of bifurcation structures of Figs. 7(a)–7(c), the set of stationary modes which interact to give westward- and eastward-propagating modes, respectively, in different parameter regimes, are related.

### 3.4. Effect of zonal advection and oceanic damping

In this section, we present the (qualitative) changes which occur in the structure of the attractors when oceanic damping and zonal advection are included. This

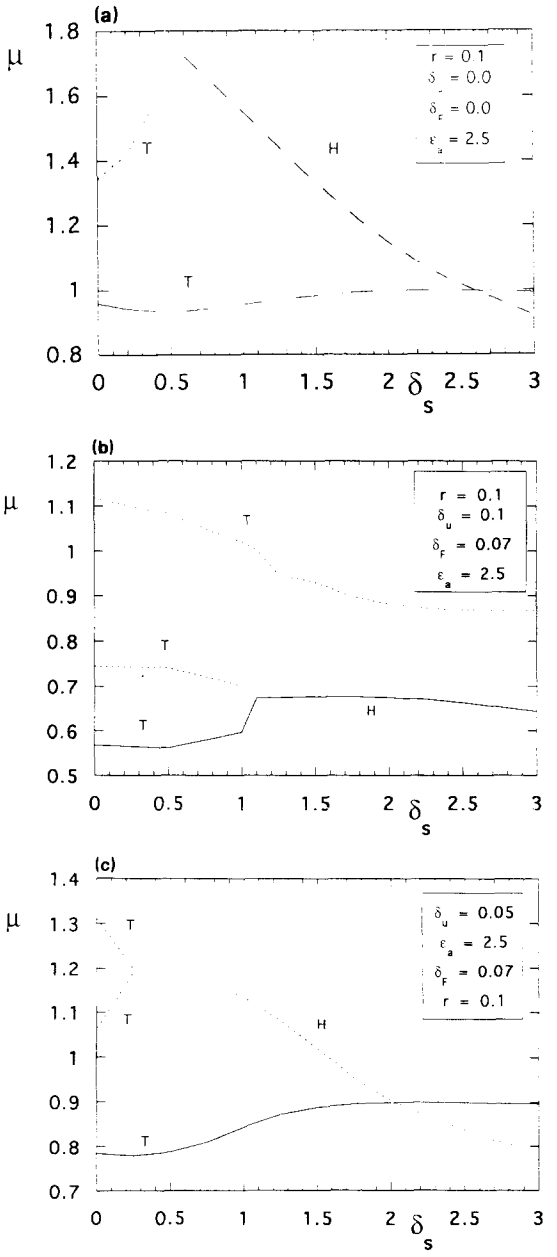


Fig. 10. Primary bifurcation structure (notation as in Fig. 2). (a) For $r = 0.1$, $\delta_u = 0$, $\delta_F^2 = 0$. (b) For $r = 0.1$, $\delta_u = 0.1$, $\delta_F^2 = 0.07$. (c) For $r = 0.1$, $\delta_u = 0.05$, $\delta_F^2 = 0.07$.

gives an impression of the sensitivity of the bifurcation structures presented above. Zonal advection contributes to the temperature structure in two ways: through the mean flow (the term $uT_x$ in (4)) and through the surface layer (the terms with $\delta_F^2$ and $\delta_u$ in (4)). We first consider the case $\epsilon_a = 2.5$, $\delta_F^2 = \delta_u = 0$ with all other parameters, except the damping rate $r$, fixed as in Table 1. Within the range of the parameters used, the climatology hardly changes with respect to that shown in Fig. 1.

The primary bifurcation structure for $r = 0.1$ is presented in Fig. 10(a). As expected, the primary bifurcation structure does not change (compared with Fig. 7(c)) when a small amount of oceanic damping is present. Only the oscillatory instabilities owing to thermocline feedback (at very low $\delta_s$) disappear, but can be brought back by changing the parameters in the subsurface temperature parameterization. When zonal advection is added (with $\delta_u = 0.1$ and $\delta_F^2 = 0.07$), the primary bifurcation picture changes (Fig. 10(b)) significantly compared with Fig. 10(a), except at the larger values of $\delta_s$. Up to $\delta_s \approx 1.2$, the first three primary bifurcations are transcritical and for intermediate values of $\delta_s$ the first two transcritical bifurcation points have merged to a Hopf bifurcation. The transition between the primary bifurcation structure of Figs. 10(a) and 10(b) is clarified by plotting this structure at an intermediate value of $\delta_u$ (Fig. 10(c)) which does have the same structure as Figs. 7(c) and 10(a). When $\delta_u$ is increased, the branch of transcritical singularities interchanges (without any interaction) with the Hopf–transcritical structure.

Zonal advection favours westward propagation and thereby these modes (associated with the Hopf bifurcation) become more unstable for larger $\delta_u$. Figs. 10(b) and 10(c) also explain why the Hopf–transcritical interaction was found by Hao et al. (1993), with zonal advection excluded, and was not found by Jin and Neelin (1993a), who included zonal advection. It also suggests that it is wisest not to let either of the two surface layer feedback terms, associated with zonal and vertical advection, respectively, go to zero without the other; for instance, using a simple $\delta_s$ for both keeps them in proportion.

## 4. Relaxation oscillations

Nonsinusoidal oscillations that evolve very slowly during part(s) of the cycle are often referred to as relaxation oscillations (Grasman, 1987). Examples of interannual oscillations deforming from relatively sinusoidal oscillations at low coupling into relaxation oscillations with a long warm phase (or in some cases, a long cold phase) were found in a simple model (Hao et al., 1993) and in the hybrid coupled model of Neelin (1990b). An example from the hybrid coupled model may be seen in Fig. 11(a), in which each cold phase is followed by a very extended warm phase. These results and the apparent association with multiply stationary states, were not previously published for lack of an adequate explanation—a reasonable explanation of the bifurcation structure can now be given.

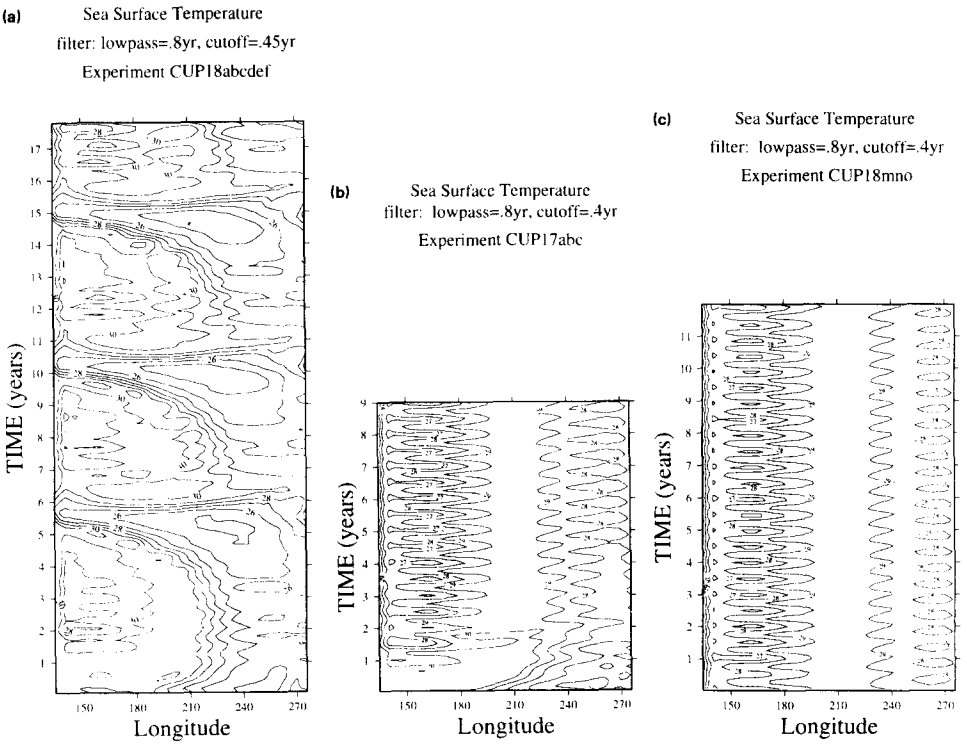


Fig. 11. (a) Evolution of the SST along the equator for a run of the HCM at relative coupling coefficient $\mu = 1.1$. A low-pass filter with a midpoint at 7 months has been applied. Initial condition is from the unstable climatological stationary point with an initial wind stress perturbation. (b) As in (a) but for $\mu = 1.2$ showing 9 years of a 18 year run. (c) As in (a) but beginning from a warm initial condition.

The model construction and the behavior which occurs at lower coupling has been described by Neelin (1990a), but is summarized here for reference. The model consists of the Geophysical Fluid Dynamics Laboratory ocean GCM, configured for the tropical Pacific basin coupled to a simple atmospheric model. Flux correction is used so there is a known climatological stationary solution created by spinning up the ocean with observed wind stress (Hellerman and Rosenstein, 1983). The atmospheric model is used as a nonlinear anomaly model for anomalies defined with respect to this ocean climatology. For the 'best estimate' atmospheric parameters, the climatology is unstable to an ENSO-like oscillation that is similar to the oscillation in Fig. 11(a), except that the warm phase is not so extended. The model ENSO cycle is also unstable to higher-frequency (5–6 month period) oscillations associated with coupled Kelvin waves, similar to those seen in Fig. 11(a). To see how the behavior evolves from simpler flow regimes, a relative coupling coefficient $\mu$ is defined (analogous to the coupling parameter used in the present model) which artificially reduces the wind stress

feedback (per unit SST anomaly) from the atmospheric model. The standard value is defined as $\mu = 1.0$. For $\mu = 0.6$, the climatology is stable, with an ENSO-like mode decaying. The primary bifurcation, at which this mode goes unstable, occurs for $\mu$ slightly less than 0.7. For a range of $\mu$ above this value, a simple limit cycle occurs (a periodic orbit); as coupling increases the amplitude of this limit cycle increases, but the period and spatial structures on the orbit do not change much. A secondary Hopf bifurcation gives the higher-frequency oscillation noted above, and the warm period already begins to lengthen by $\mu = 1.0$. The results at coupling larger than standard are shown here. Fig. 11(a) shows the case for $\mu = 1.1$ but otherwise exactly like the standard case $\mu = 1.0$. The relaxation oscillation has a period of about 5 years where the warm phase of the cycle is lengthened considerably compared with the cycle at lower coupling, whereas the length of the cold phase remains approximately the same.

When the coupling is increased to $\mu = 1.2$, the ENSO-like oscillations disappear and are replaced by an eternal warm phase, as seen in Fig. 11(b) for a run with the same initial conditions as Fig. 11(a). This run was continued stably in the warm state for another 9 years beyond what is shown. The Kelvin-wave oscillations continue, but now occur about the warm stationary point instead of about the ENSO limit cycle. The warm state is maintained by westerly wind anomalies which almost cancel the climatological wind stress imposed by flux correction. The equatorial upwelling is thus largely shut off and the east–west thermocline gradient tends to flatten, resulting in SST anomalies that nearly cancel the climatological cold tongue; these in turn maintain the wind stress. The coupled feedbacks thus create an alternate stationary state in which ocean dynamics are much less active than in the state constructed by flux-correction. Similar dynamics, but to a lesser degree, are found in the lengthened warm phase of Fig. 11(a), which is why it evolves so slowly. One can also test for the existence of this warm stationary point at lower coupling: Fig. 11(c) shows a case with $\mu = 1.1$, identical to the run of Fig. 11(a) except that the initial conditions are taken from the warm state of Fig. 11(b). The warm state persists over a length of time which is large compared with the period of the limit cycle and the typical adjustment times of the system. This strongly suggests that the warm stationary point exists and is stable, i.e. there are two attractors, the warm state and the ENSO cycle for this value of coupling.

In this section we show how such a relaxation oscillation arises dynamically when the thermocline feedback is dominant (small $\delta_s$). To obtain reasonable values of the period, the coefficients in the subsurface temperature parameterization were changed to $\eta_1 = 4$, $\eta_2 = 0.6$. For $\delta_s = 0.5$, $\alpha = 0.5$, $\epsilon_w = 0.428$ and $\epsilon_a = 2.5$, the bifurcation diagram is shown in Fig. 12(a). This bifurcation diagram arises in the same way as that for $\delta_s = 0$ in Fig. 8(b). A Hopf bifurcation is present at $\mu = 1.684$ and a saddle node bifurcation at $\mu = 2.169$. In Fig. 12(b), the periodic orbits are shown along the branch which leads from the Hopf to the saddle node by plotting the time evolution of the temperature at the east coast for different $\mu$. With increasing $\mu$, the cold state becomes longer and the system evolves quickly through the warm state. For $\mu$ larger than the value at the saddle node, a steady (cold) state is reached.

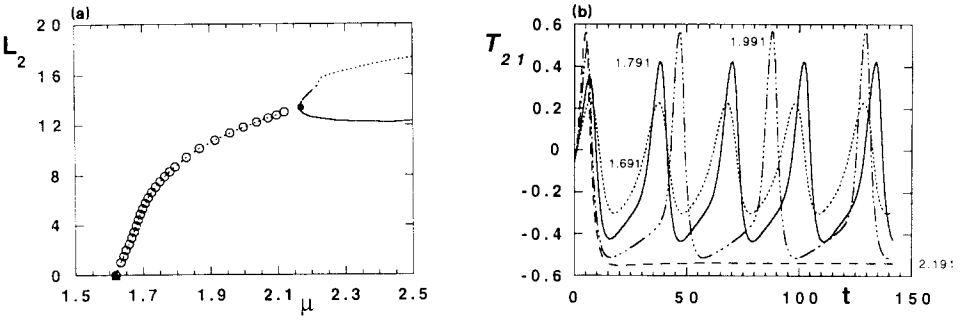


Fig. 12. (a) Bifurcation picture for $\delta_s = 0.3$, $\epsilon_a = 2.5$, using the $L_2$ norm of the solution as ordinate. The branch marked by open circles represents a periodic orbit. (b) Time dependence of the temperature perturbation at the east coast for several values of $\mu$.

A sketch of the dynamics of this limit cycle–saddle node interaction at $\mu = \mu_c$ in phase space is presented in Fig. 13. Equilibrium points are shown as dots, the circle represents the limit cycle and the curves indicate trajectories. For $\mu < \mu_c$ (Fig. 13(a)), only the limit cycle (arising from the Hopf bifurcation) enclosing an unstable equilibrium (the climatology) is present. Nearby is a region where there

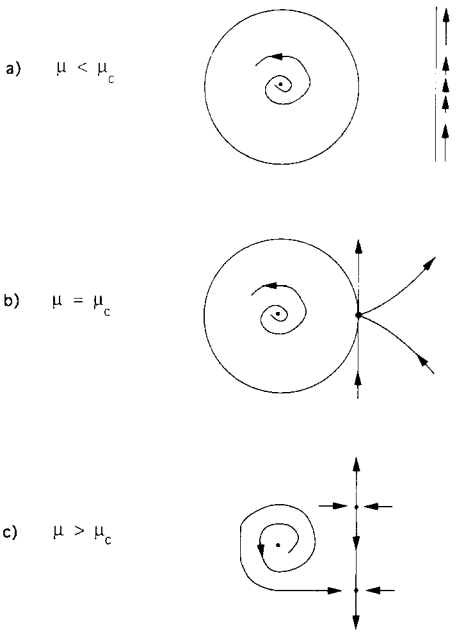


Fig. 13. Schematic diagram of the local dynamics in phase space near the saddle-node–limit cycle interaction at $\mu = \mu_c$. Arrows indicate direction of trajectories (with small arrows indicating slow regions of flow, where necessary). Dots indicate equilibria. (a) $\mu < \mu_c$. (b) $\mu = \mu_c$. (c) $\mu > \mu_c$.

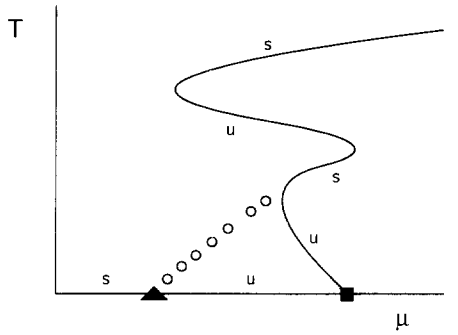


Fig. 14. Plausible bifurcation picture of the dynamics explaining the relaxation oscillation in the HCM results as shown in Fig. 11. Curves indicate stationary solutions; line of open dots indicates oscillatory solutions.

are no equilibria but the flow slows down, because other equilibria are present at slightly larger values of $\mu$. The critical structure for $\mu = \mu_c$ is shown in Fig. 13(b), where the limit cycle connects to the saddle node. At slightly larger $\mu$ (Fig 13(c)) three equilibria appear, of which only one is stable (the cold state), and the limit cycle has ceased to exist.

Hence, as the limit cycle increases in amplitude (with increasing $\mu$), the length of the cold phase increases because of the presence of the stable steady cold branch at larger coupling. As trajectories pass close to this stationary point, the flow is necessarily slow. On the other hand, the period remains finite and the other (warm) phase of the oscillation is therefore relatively fast. A limit cycle–saddle node interaction might also explain the relaxation oscillation as presented in Fig. 11. What is required in addition to Fig. 12(a) is the existence of another steady state at a coupling interval enclosing the limit cycle–saddle node interaction (Fig. 14). Because of the bifurcation diagrams already encountered (see e.g. Fig. 8(a)) this seems reasonable.

## 5. Results for $\delta = 1$: effects of ocean wave dynamics

We return now to the standard case in Section 3, i.e. with $r = 0$, $\delta_\mu = 0$ and $\delta_F^2 = 0$. To show how $\delta \neq 0$ affects the stability of the climatology (Fig. 1), we consider the simplest case $\epsilon_a = 0$. For $\delta_s = 1$, the growth factors $\lambda$ are shown for three different values of $\delta$ in Fig. 15(a). In agreement with Fig. 2(a), both growth factors are real for $\delta = 0$ and $\mu > 0$ and increase nearly linearly with $\mu$. At smaller $\mu$, a two-degeneracy is present, and the eigenvalues become complex conjugate. As soon as $\delta \neq 0$, a two-degeneracy occurs at large $\mu$ which induces oscillatory instabilities at large coupling and which depends on time scales of ocean dynamics. This second two-degeneracy (Fig. 15(a)) shifts to smaller values of $\mu$ as $\delta$ is increased. The range of values of $\mu$ where ocean dynamics is essential to the oscillations thereby becomes larger.

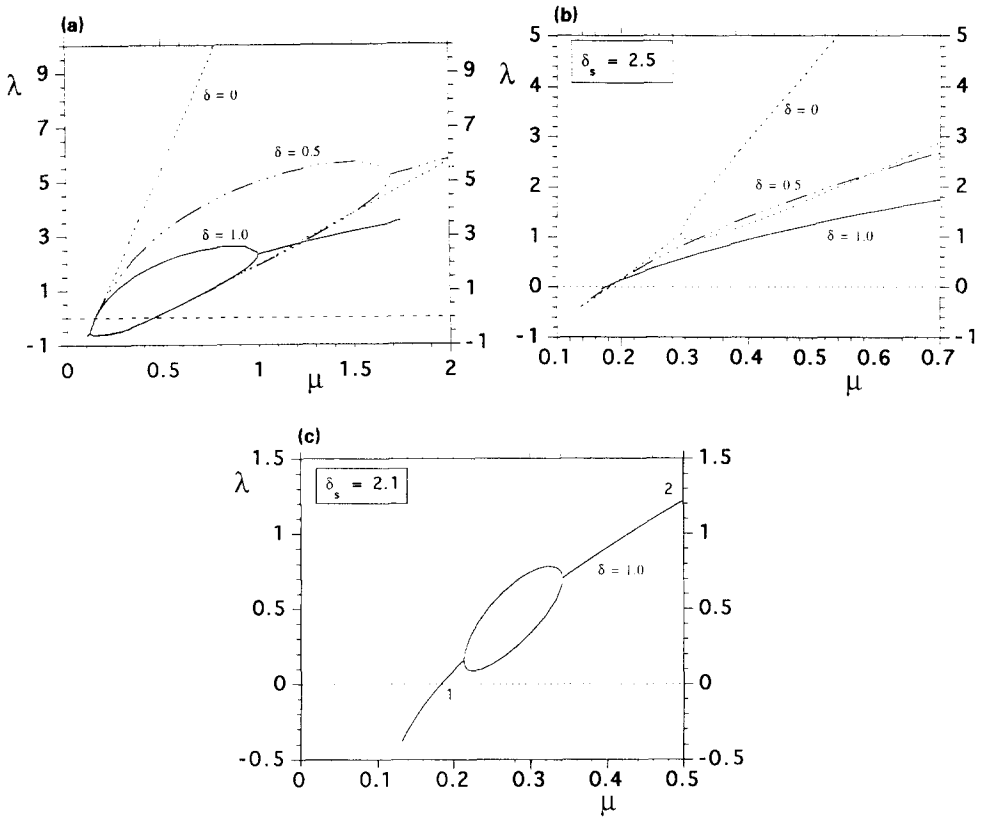


Fig. 15. (a) Growth factor $\lambda = \mathrm{Re}(\sigma)$ as a function of $\mu$ for $\epsilon_a = 0.0$, $\delta_s = 1.0$ and three values of $\delta$. (b) Same as (a) but for $\delta_s = 2.5$. (c) Same as (a) but for $\delta_s = 2.1$ and showing only $\delta = 1$.

From Fig. 2(a), we know that for $\delta = 0$ at larger $\delta_s$ the primary bifurcation point is of Hopf type (westward-propagating). As shown in Fig. 15(b), this is due to an upward shift of the two-degeneracy such that the oscillatory part of the branch becomes the primary instability. At larger $\mu$, the instabilities are still stationary. However, for $\delta = 1$ no stationary instabilities exist any longer in the computational domain. A picture of the eigenvalue branch at $\delta_s = 2.1$ (Fig. 15(c)) shows that the two two-degeneracies, one associated with the westward-propagating SST mode and one associated with oscillation owing to wave dynamics, move to each other as $\delta_s$ is increased. They finally merge at $\delta_s \approx 2.3$ in a three-degeneracy. At slightly larger $\delta_s$, the frequency associated with the oscillatory instability no longer goes to zero but passes through a minimum and increases again with larger $\mu$. The transition from a stationary (at $\delta = 0$) to a propagating regime (at $\delta = 1$) therefore occurs smoothly, e.g. at $\mu = 0.5$ (Fig. 15(b)); this confirms the results in Jin and Neelin (1993a), who explored this regime. In addition, at smaller values of $\mu$, the transition from a regime dominated by propagation to a regime where subsurface

memory is dominant also occurs smoothly. The eigenvector structures at both sides of the three-degeneracy are only slightly different. At Point 1 in Fig. 15(c), the structure resembles the SST oscillatory mode in the fast-wave limit (e.g. of Fig. 6). At Point 2, the SST pattern is fairly similar to that at Point 1, but the thermocline depth pattern is somewhat altered owing to the time scales of ocean adjustment.

## 6. Discussion

In this paper, we determined stable and unstable steady states of an intermediate coupled ocean–atmosphere model. The types of dynamical behavior are basically those discussed by Hao et al. (1993) and Jin and Neelin (1993a), but the bifurcation pictures show exactly how this dynamics is established in parameter space. Complex dynamics can be understood through simpler structures by unfolding them in parameter space. The knowledge of the unstable branches of steady states, which are 'hidden' in a time-integration, is important to understand this dynamics. In this aspect, the results add greatly to those obtained by time integration.

The climatology can become unstable at sufficiently large coupling, owing to both stationary and oscillatory instabilities. The results show the importance of the first two primary bifurcation points for the qualitative dynamics of the system. Because of the lack of symmetry of the system, there are generically three situations, T–T, T–H or H–T, where T stands for transcritical and H for Hopf bifurcation points; for instance, T–H denotes the case where the first mode to go unstable is purely growing, leading to other stationary solution branches through transcritical bifurcation, whereas at the second bifurcation oscillatory modes go unstable.

If the first primary bifurcation from the climatology is transcritical, there exist at least two stable branches of steady states for an interval of coupling values $\mu$. One of these branches is stable already for values of $\mu$ smaller than that at the primary bifurcation point. This implies that finite amplitude disturbances can bring the system into a new steady state, even though the original climatology is linearly stable. This type of subcritical instability is very likely to occur in more sophisticated models, because whenever a constructed climatological stationary branch goes unstable to a stationary mode, a transcritical bifurcation is expected generically (owing to lack of symmetry in the vector field associated with such a model). Both stable steady states can be thought of as a climatology modified through coupling. It appears that this modification typically occurs in two ways: a shut-off of the cold tongue (through weakening of the upwelling and deepening of the thermocline in the eastern part of the basin, yielding a warm state), or a shift of the cold tongue to the center of the basin.

In areas of parameter space with a T–T primary structure, a secondary branch of steady states containing a Hopf bifurcation connects both T points. This behavior is typically found at small $\epsilon_a$ and small $\delta_s$. The secondary Hopf moves on

the primary branch either with increasing $\delta_s$ (at small $\epsilon_a$) or with decreasing $\delta_s$ (at large $\epsilon_a$). In either case, the competition between two stationary modes, a coupling of two spatial degrees of freedom, is the origin of the westward- or eastward-propagating oscillatory instabilities, respectively.

This mode competition provides an economical view of the relation between eastward- and westward-propagating oscillations, which occur in their respective parameter ranges. Only a few solution branches are involved in the structures in parameter space that combine stationary modes to produce a westward-propagating mode in one region and an eastward-propagating mode in another region. Thus, only a few spatial degrees of freedom are important in any one region (although the spatial structure of a given mode may also evolve smoothly as a function of a parameter, so the spatial degrees of freedom cannot be reduced a priori in the model). One might say that the same few modes are 'recycled' in different combinations according to the changes in relative importance of various physical processes. For instance, when the first two bifurcations are both transcritical, the mode with the largest spatial scale is the first to go unstable, followed by the second mode, which has slightly smaller spatial scale and different spatial phase (e.g. as measured by the position of the extremum or zero crossing). In the case of intermediate values of $\delta_s$ (see Fig. 2(b)), the two competing physical processes are the surface-layer feedback and the thermocline feedback. Although both favor large-scale instabilities owing to the atmospheric response (Jin and Neelin, 1993a), the thermocline feedback depends on an integral over the wind stress and therefore favors large scales more strongly. As $\delta_s$ is increased, the role of the surface-layer feedbacks is enhanced and thus the second, smaller-scale mode catches up to the first, allowing the two spatial degrees of freedom to merge into a westward-propagating solution.

This view is complementary to the discussion by Hao et al. (1993) based on the analogy between propagating modes in the finite basin case and those of the periodic basin case considered by Neelin (1991). The latter can provide physical intuition for the regimes where the modes are clearly propagating, but this analysis provides a much clearer picture of what happens in the stationary regimes in between. Furthermore, it permits understanding of cases where the bifurcation structure appears sensitive to small perturbations of the model. We provide an example by comparing the case where the parameter governing zonal advection is set to zero with the case where it is held constant while the parameter governing upwelling is varied from zero to normal values. The bifurcation structure changes significantly with the zonal advection compared with the case without. However, the relation between the two cases can be understood by examining intermediate cases, both in terms of the interchange of solution branches and in physical terms, as the zonal advection maintains a westward-propagating tendency at smaller values of the upwelling feedback.

A similar connection may be made between the stationary solutions and the oscillatory instabilities that arise from the time scales of ocean dynamical adjustment such as those in Cane–Zebiak type models (Zebiak and Cane, 1987; Battisti and Hirst, 1989). A simple structure in parameter space links the westward-propa-

gating SST mode, two stationary SST modes and the mode depending on ocean dynamics, in a manner consistent with that conjectured by Jin and Neelin (1993a).

In areas where the primary structure is H–T, relaxation oscillations may be found as an interaction between a limit cycle and a saddle node. This is a striking example where nearby attractors in parameter space are needed to explain the dynamics. In areas where the primary structure is T–H, Hopf–steady-state interactions and (associated with them) torus bifurcations may occur. These results are expected to be relevant to a class of flux-corrected models, including intermediate models, hybrid coupled models and possibly flux-corrected GCMs. We provide an example with a hybrid coupled model to illustrate how complex structures analogous to those found here can influence the time-dependent solutions, even when the structures are not directly inferrable from the time-dependent solution alone. These results suggest that certain types of sensitivity in such models may be associated with the presence of additional stationary solutions. Furthermore, laying bare the structure of the stationary solutions in parameter space, and the physical structure of the unstable modes that gives rise to them, helps to inform our intuition about how plausible it is that multiple stationary states can play a role in the observed tropical climate system. The fact that these solutions arise as transcritical bifurcations, and that they modify a prescribed climate state by mechanisms similar to that which should maintain it in the absence of flux correction, led us to conjecture that they were not likely to persist when flux correction is relaxed, and this has turned out to be the case (Neelin and Dijkstra, 1995). The mapping of stationary solutions presented here thus has two main punchlines: on the one hand, it diagnoses a complex and potentially problematic feature of flux-corrected models; and on the other, it provides a rather complete picture of how the important (and robust) oscillatory solutions connect to each other in these models.

## Acknowledgments

An earlier description of the hybrid coupled model (HCM) results was given by Neelin (1990b). Thanks are due to W. Weibel for computational assistance and data analysis on the HCM runs; these were carried out at the National Center for Atmospheric Research under support from NSF Grants ATM-9215090 and ATM-9349726. All further computations were performed on the CRAY Y-MP at the Academic Computer Centre (SARA), Amsterdam. Use of these computing facilities was sponsored by the Stichting Nationale Supercomputer Faciliteiten (National Computing Facilities Foundation, NCF) with financial support from the Nederlandse Organisatie voor Wetenschappelijk Onderzoek (Netherlands Organization for Scientific Research, NWO) within Project SC-283. One of authors (H.A.D.) thanks Will de Ruijter (IMAU, University of Utrecht) for much encouragement and support.

## Appendix A: Details of the coupled model and expressions of dimensionless parameters in Eq. (4)

In the ocean model, the surface layer velocities $u_s$, $v_N$ and $w_s$ are parameterized as

$$u_s = b_u[\tau/(\rho H)]$$

$$w_s = -b_w[\tau/(\rho H)] + H_1 b_u \frac{\partial}{\partial x}[\tau/(\rho H)]$$

$$v_N = -(L_y/2H_1) b_w[\tau/(\rho H)]$$

where $b_u$ and $b_w$ are constants. The subsurface temperature is parameterized as a function of $h$ as done by Hao et al. (1993), e.g.

$$T_s(h) = T_{s0} + (T_0 - T_{s0}) \tanh[(h + h_0)/H^*]$$

where $h_0$ is some offset value, $T_0$ is the equilibrium temperature in absence of dynamics and $\epsilon_T$ the related damping coefficient, $T_{s0}$ is the subsurface temperature for $h = -h_0$ and $H^*$ controls the steepness of the transition if $h$ passes through $-h_0$. In this way, the range of the subsurface temperature is given by $[2T_{s0} - T_0, T_0]$.

The steady-state mean velocity fields and thermocline displacements in (3) can be solved in terms of $T$ with the result

$$h(T; x) = \left\{ \int_0^1 f_1(\phi\xi) G(T; \xi)\, d\xi f_3[\phi(x-1)] - \int_x^1 G(T; \xi) f_3[\phi(x-\xi)]\, d\xi \right\}$$

$$u(T; x) = -i\left\{ \int_0^1 f_1(\phi\xi) G(T; \xi)\, d\xi f_2[\phi(x-1)] - \int_x^1 G(T; \xi) f_2[\phi(x-\xi)]\, d\xi \right\}$$

with $G(T; x) = F_0 F(x) + \mu A(T; x)$, $\phi = -ir$ and

$$f_1(\phi x) = \left( \frac{\sin(2\phi x)}{\sin(2\phi)} \right)^{1/2}$$

$$f_2(\phi x) = [\cos(2\phi x)]^{-1/2} \sin(2\phi x)$$

$$f_3(\phi x) = [\cos(2\phi x)]^{1/2}$$

With the scaling as mentioned in Section 2.1, the expressions for the parameters in Eq. (4) are

$$\alpha = \frac{H_1}{\tilde{H}}, \qquad \delta_s = \frac{b_w c_0}{\tilde{H}}, \qquad \epsilon_w = \frac{\epsilon_T L}{c_0}$$

$$\delta_F^1 = F_0 \delta_s \alpha^{-1}, \qquad \eta_1 = \frac{H}{H^*}, \qquad \eta_2 = \frac{h_0}{H^*}, \qquad \delta_F^2 = \delta_u F_0, \qquad \delta_u = \frac{b_u c_0}{L}$$

## Appendix B: Expressions of coefficients in basic state equation, Eq. (5)

$$a_1(x) = \delta_F^2 F(x) + \bar{u}(x)$$
$$d_1(x) = \epsilon_w + b_1(x) + c_1(x)$$
$$d_2(x) = \epsilon_w \mathrm{T}_0 + b_1(x)\mathrm{T}_s\left[\bar{h}(x)\right] + c_1(x)\mathrm{T}_N$$

with

$$b_1(x) = \tfrac{1}{2}\left(1 + \tanh\left\{\epsilon^{-1}\left[\delta_F^2 F'(x) - r\bar{\mathrm{h}}(x) - \delta_F^1 F(x)\right]\right\}\right)$$
$$\cdot\left[\alpha\delta_F^2 F'(x) - \alpha r\bar{\mathrm{h}}(x) - \alpha\delta_F^1 F(x)\right]$$
$$c_1(x) = \tfrac{1}{2}\left\{1 + \tanh\left[\epsilon^{-1}\delta_F^1 F(x)\right]\right\}\cdot\alpha^{-1}\delta_F^1 F(x)$$

## Appendix C: Expressions for the coefficients in the linear stability problem

The perturbation zonal velocity $u$ and thermocline depth $h$ can be expressed in terms of the temperature perturbation $T$ through

$$u(T;x) = -i\mu\left\{\int_0^1 f_1(\phi\zeta)A(T;\zeta)\,\mathrm{d}\zeta f_3[\phi(x-1)]\right.$$
$$\left. - \int_x^1 A(T;\zeta)f_3[\phi(x-\zeta)]\,\mathrm{d}\zeta\right\}$$
$$h(T;x) = \mu\left\{\int_0^1 f_1(\phi\zeta)A(T;\zeta)\,\mathrm{d}\zeta f_3[\phi(x-1)]\right.$$
$$\left. - \int_x^1 A(T;\zeta)f_2[\phi(x-\zeta)]\,\mathrm{d}\zeta\right\}$$

where $\phi = -i(\sigma\delta + r)$ and the functions $f_i$ are the same as in Appendix A. The coefficients in Eq. (8) are given as follows. With $f(z) = \frac{1}{2}[1 + \tanh(z/\epsilon)]$, $f'(z) = (1/2\epsilon)\cosh^{-2}(z/\epsilon)$ and $g(h) = \partial T_s/\partial h$, we define

$$\alpha_1(x) = -f\left[-\delta_F^1 F(x)\right]\cdot\alpha\delta_F^1 F(x)$$
$$\alpha_2(x) = \bar{\mathrm{T}}(x) - \mathrm{T}_s\left[\bar{\mathrm{h}}(x)\right]$$
$$\alpha_3(x) = f'\left[-\alpha\delta_F^1 F(x)\right]\cdot\delta_F^1 F(x)$$
$$\beta_1(x) = f\left[\delta_F^1 F(x)\right]\cdot\delta_F^1 F(x)$$
$$\beta_2(x) = \bar{\mathrm{T}}(x) - \mathrm{T}_N$$
$$\beta_3(x) = f'\left[\alpha\delta_F^1 F(x)\right]\cdot\delta_F^1 F(x)$$
$$\gamma_1(x) = g\left[\bar{\mathrm{h}}(x)\right]$$

and the coefficients become

$$\epsilon_w(x) = \epsilon_w + \alpha_1(x) + \beta_1(x)$$
$$\gamma(x) = \alpha_1(x) \cdot \gamma_1(x)$$
$$b(x) = \left\{f\left[-\delta_F^1 F(x)\right] + \alpha_3(x)\right\} \cdot \alpha_2(x) - \alpha^{-1}\beta_2(x) \cdot \left\{f\left[\delta_F^1 F(x)\right] - \beta_3(x)\right\}$$

## Appendix D: Numerical details

Both steady solutions and periodic solutions can be computed within AUTO (Doedel, 1980). Steady solutions T($x$) of (4) are computed as follows. On an equidistant grid in $x$, $x_j = (j-1)\,\Delta x$, j = 1,..., $M$, $(M-1)\Delta x = 1$, we let $u_j = T(x_j)$, $j = 1,\ldots,M$. By evaluating Eq. (4) at each grid point we obtain a system of nonlinear algebraic equations $\boldsymbol{G_M}(\boldsymbol{u}, \boldsymbol{p}) = 0$, with a straightforward definition of the mapping $\boldsymbol{G_M}$: $\mathbb{R}^M \times \mathbb{R}^3 \to \mathbb{R}^M$ and where $\boldsymbol{p} = (\epsilon_a, \delta_s, \mu)^T$ is the vector of parameters. The accuracy set in AUTO is

$$|\Delta\chi|/(1 + |\Delta\chi|) < \epsilon_\chi, \quad |\Delta\boldsymbol{u}|_\infty/(1 + |\Delta\boldsymbol{u}|_\infty) < \epsilon_u$$

where $\chi$ and $\boldsymbol{u}$ denote a (free) parameter and the solution vector, respectively. In the calculations reported, $\epsilon_\chi = \epsilon_u = 10^{-6}$ was used.

A similar approach is taken to compute the complex growth factors $\sigma$ determining the stability of a certain steady state. If

$$T_j^R = \mathrm{Re}\left[\tilde{T}(x_j)\right] \text{ and } T_j^I = \mathrm{Im}\left[\tilde{T}(x_j)\right]$$
$$\lambda = \mathrm{Re}(\sigma), \qquad \nu = \mathrm{Im}(\sigma)$$

then the eigenvalue problem determining the stability of the basic state can be written as a nonlinear system of algebraic equations $\boldsymbol{F_M}(\boldsymbol{y}) = 0$, where

$$\boldsymbol{y} = \left(T_1^R, \ldots, T_M^R, T_1^I, \ldots, T_m^I, \lambda, \nu\right)$$

and a mapping $\boldsymbol{F_M}$: $\mathbb{R}^{2M+2} \to \mathbb{R}^{2M+2}$, for which $2M$ equations are obtained by forcing (8) at each grid point and the other two equations arise through the normalization of real and complex part of the eigenvector. This system of algebraic equations is solved again with the AUTO code.

## References

Battisti, D.S. and Hirst, A.C., 1989. Interannual variability in a tropical atmosphere–ocean model: influence of the basic state, ocean geometry and nonlinearity. J. Atmos. Sci., 46: 1687–1712.

Cane, M.A., Münnich, M. and Zebiak, S.E., 1990. A study of self-excited oscillations of the tropical ocean–atmosphere system. Part I: Linear analysis. J. Atmos. Sci., 47: 1562–1577.

Chow, S.N. and Hale, J.K., 1982. Methods of Bifurcation Theory. Springer, Heidelberg.

Doedel, E., 1980. AUTO: A program for the automatic bifurcation analysis of autonomous systems. In: Proc. 10th Manitoba Conf. on Numerical Maths and Comput., 30: 265–274.

Gill, A.E., 1980. Some simple solutions for the heat-induced tropical circulation. Q. J. R. Meteorol. Soc., 106: 447–462.

Golubitsky, M., Steward, I. and Schaeffer, D.G., 1988. Singularities and Groups in Bifurcation Theory, Vol. II. Springer, Heidelberg.

Grasman, J., 1987. Asymptotic Methods for Relaxation Oscillations and Applications. Springer, Heidelberg.

Guckenheimer, J. and Holmes, P., 1983. Nonlinear Oscillations, Dynamical Systems and Bifurcations of Vector Fields. Springer, Heidelberg.

Hao, Z., Neelin, J.D. and Jin, F.F., 1993. Nonlinear tropical air–sea interaction in the fast-wave limit. J. Climate, 6: 1523–1544.

Hellerman, S. and Rosenstein, M., 1983. Normal monthly windstress over the world ocean with error estimates. J. Phys. Oceanogr., 13: 1093–1104.

Hirst, A.C., 1986. Unstable and damped equatorial modes in simple coupled ocean–atmosphere models. J. Atmos. Sci., 43: 606–630.

Hirst, A.C., 1988. Slow instabilities in tropical ocean basin–global atmosphere models. J. Atmos. Sci., 45: 830–852.

Hirst, A.C. and Lau, K.M., 1990. Intraseasonal and interannual oscillations in coupled ocean–atmosphere models. J. Climate, 3: 713–715.

Jin, F.F. and Neelin, J.D., 1993a. Modes of interannual tropical ocean–atmosphere interaction—a unified view. Part I: Numerical results. J. Atmos. Sci., 50: 3477–3503.

Jin, F.F. and Neelin, J.D., 1993b. Modes of interannual tropical ocean–atmosphere interaction—a unified view. Part III: Analytical results in fully coupled cases. J. Atmos. Sci., 50: 3523–3540.

Langford, W.L., 1979. Periodic and steady-state mode interactions lead to tori. SIAM J. Appl. Math., 37: 22–45.

Münnich, M., Cane, M.A. and Zebiak, S.E., 1991. A study of self-excited oscillations of the tropical ocean–atmosphere system. Part II: Nonlinear cases. J. Atmos. Sci., 48: 1238–1248.

Neelin, J.D., 1990a. A hybrid coupled general circulation model for El Niño studies. J. Atmos. Sci., 47: 674–693.

Neelin, J.D., 1990b. Bifurcations and El-Niño in a hybrid coupled GCM. In: Proceedings of the 14 Climate Diagnostics Workshop, Climate Analysis Center, NOAA, Washington, DC, pp. 22–27.

Neelin, J.D., 1991. The slow sea surface temperature mode and the fast-wave limit: analytic theory for tropical interannual oscillations and experiments in a hybrid coupled model. J. Atmos. Sci., 48: 584–606.

Neelin, J.D. and Dijkstra, H.A., 1995. Coupled ocean–atmosphere models and the tropical climatology, part I: The dangers of flux-correction. J. Climate, in press.

Neelin, J.D. and Jin, F.F., 1993. Modes of interannual tropical ocean–atmosphere interaction—a unified view. Part II: Analytical results in the weak-coupling limit. J. Atmos. Sci., 50: 3504–3522.

Philander, S.G.H., 1989. El-Niño and the Southern Oscillation. Academic Press, New York.

Rasmusson, E.M., Wang, X. and Ropelewski, C.F., 1990. The biennial component of ENSO variability. J. Mar. Syst., 1: 71–96.

Schopf, P.S. and Suarez, M.J., 1988. Vacillations in a coupled ocean–atmosphere model. J. Atmos. Sci., 45: 549–566.

Schopf, P.S. and Suarez, M., 1990. Ocean wave dynamics and the time scale of ENSO. J. Phys. Oceanogr., 20: 629–645.

Suarez, M.J. and Schopf, P.S., 1988. A delayed action oscillator for ENSO. J. Atmos. Sci., 45: 3283–3287.

Wakata, Y. and Sarachik, E.S., 1991. Unstable coupled atmosphere–ocean basin modes in the presence of a spatially varying basic state. J. Atmos. Sci., 48: 2060–2077.

Zebiak, S.E. and Cane, M.A., 1987. A model El Niño–Southern Oscillation. Mon. Weather Rev., 115: 2262–2278.